

# Co-phasing of a diluted aperture synthesis instrument for direct imaging

## II. Experimental demonstration in the photon-counting regime with a temporal hypertelescope

L. Bouyeron<sup>1,2</sup>, L. Delage<sup>1</sup>, R. Baudoin<sup>1,3</sup>, J. T. Gomes<sup>1</sup>, L. Grossard<sup>1</sup>, and F. Reynaud<sup>1</sup>

<sup>1</sup> Équipe photonique – XLIM (CNRS UMR 7252), University of Limoges, 123 avenue Albert Thomas, 87060 Limoges Cedex, France  
e-mail: laurent.bouyeron@unilim.fr

<sup>2</sup> CODECHAMP, 23190 Champagnat, France

<sup>3</sup> LEUKOS SAS, 87069 Limoges Cedex, France

Received 15 March 2013 / Accepted 7 April 2014

### ABSTRACT

**Context.** Amongst the new techniques currently developed for high-resolution and high-dynamics imaging, the hypertelescope architecture is very promising for direct imaging of objects such as exoplanets. The performance of this instrument strongly depends on the co-phasing process accuracy. In a previous high-flux experimental study with an eight-telescope array, we successfully implemented a co-phasing system based on the joint use of a genetic algorithm and a sub-aperture piston phase diversity using the object itself as a source for metrology.

**Aims.** To fit the astronomical context, we investigate the impact of photon noise on the co-phasing performance operating our laboratory prototype at low flux. This study provides experimental results on the sensitivity and the dynamics that could be reached for real astrophysical observations.

**Methods.** Simulations were carried out to optimize the critical parameters to be applied in the co-phasing system running in the photon-counting regime. We used these parameters experimentally to acquire images with our temporal hypertelescope test bench for different photon flux levels. A data reduction method allows highly contrasted images to be extracted.

**Results.** The optical path differences have been servo-controlled over one hour with an accuracy of 22.0 nm and 15.7 nm for 200 and 500 photons/frame, respectively. The data reduction greatly improves the signal-to-noise ratio and allows us to experimentally obtain highly contrasted images. The related normalized point spread function is characterized by a  $1.1 \times 10^{-4}$  and  $5.4 \times 10^{-5}$  intensity standard deviation over the dark field (for 15 000 snapshots with 200 and 500 photons/frame, respectively).

**Conclusions.** This laboratory experiment demonstrates the potential of our hypertelescope concept, which could be directly transposed to a space-based telescope array. Assuming eight telescopes with a 30 cm diameter, the *I*-band limiting magnitude of the main star would be 7.3, allowing imaging of a companion with a 17.3 mag.

**Key words.** instrumentation: high angular resolution – instrumentation: interferometers – techniques: interferometric

### 1. Introduction

The hypertelescope concept (Labeyrie 1996) is a promising concept for the next generation of high angular resolution instruments. The main feature of this multi-aperture interferometer is to provide direct images in the milliarcsecond range at optical wavelengths. For this purpose, the hypertelescope allows isolation of the light of each resolved element of the object on one pixel of the image. The related potential astrophysical targets can be extended sources and binary systems with high contrasts. For example, in the case of an exoplanetary system, the photons coming from the faint companion are always imaged separately from the main bright source. Thanks to this property, this instrument shows a higher sensitivity than a classical interferometer (Lawson 1997; Ten Brummelaar et al. 2005; Petrov et al. 2007) sampling the spatial spectrum of the object. However, the expected performance strongly depends on the accuracy of the co-phasing system.

In 2007, we proposed an alternative hypertelescope architecture (Reynaud & Delage 2007) called the temporal hypertelescope (THT). The main advantage of this instrument is its

versatility. It can be easily reconfigured to fit the observed object geometry, and is well suited for spatial and terrestrial instruments. A THT test bench was implemented at the XLIM laboratory (Bouyeron et al. 2010) thanks to the support of CNES and Thales Alenia Space. This instrument consists of eight telescopes linked to an integrated-optics eight-to-one interferometer through optical fibres. In a previous step (Bouyeron et al. 2012), we developed a co-phasing method based on a joint use of a genetic algorithm (GA, Brady 1985) and the sub-aperture piston phase diversity technique (SAPPD, Bolcar & Fienup 2005, 2009). This method relies on the use of the current image and an aberrated one in order to infer the instrument phase without any a priori knowledge on the observed object. This phase shift is used as an error signal and is sent to the feedback loop dedicated to the co-phasing of the instrument. We experimentally obtained a  $\lambda/400$  (4 nm) stabilization of the optical path difference over one hour, allowing the acquisition of high-contrast images (1:10 000). However, this first experiment was realized using sources much brighter than available astronomical objects. Consequently, the impact of photon noise on the co-phasing system was not significant.

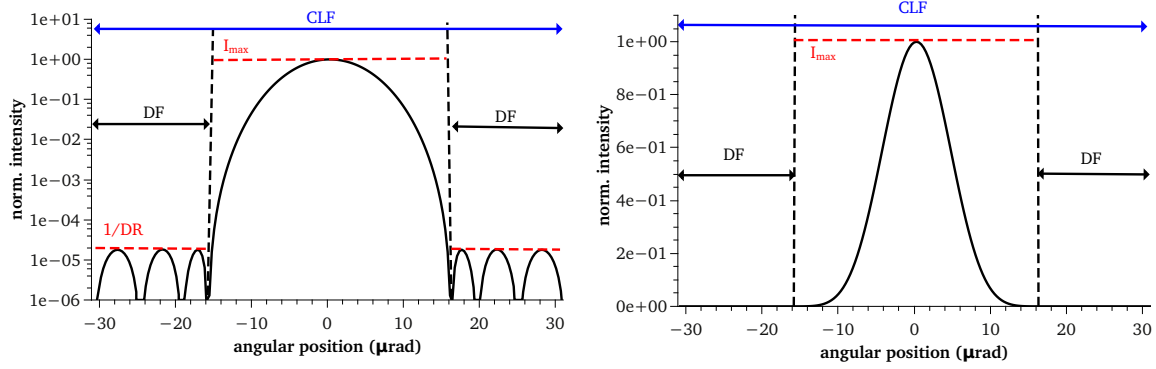


**Fig. 1.** THT test-bench theoretical PSF on logarithmic (*left*) and linear (*right*) scale. In both cases, the intensity is normalized. The telescope-array configuration is optimized for high-contrast imaging. DR is the dynamic range of the PSF, CLF is the clean field of view and DF is the dark field.

In this article, we address this last point and report on experimental co-phasing results obtained in the photon-counting regime (PCR) with the THT test bench. Dynamic and point spread function (PSF) measurements are achieved using a double output interferometer. The first one operates at low flux and is used to stabilize the optical paths of the instrument. The second one displays the image in a high flux regime and is used as a reference measurement to check the co-phasing accuracy. The experimental setup is described in Sect. 2. The optimization of the phase-shift evaluation (SAPPD parameters) involved in the co-phasing process in the photon-counting regime is presented in Sect. 3 through simulations. Section 4 presents the experimental tests of the co-phasing process and image acquisitions obtained with the THT instrument operating in the photon-counting regime. Finally, using our experimental data as a starting point, the extrapolations of these results to a real space-based instrument are presented in Sect. 5.

## 2. General description of the THT test bench

A THT is a multi-aperture interferometer providing a direct image of the observed object. The instrument is based on an experimental configuration able to maintain the phase relationship between the optical fields coming from the telescopes and to be mixed in accordance with the golden rule of imaging interferometry (Traub 1986). In the THT (Reynaud & Delage 2007), these phases are temporally modulated, taking the input pupil configuration into account. The image is temporally acquired point by point through a raster scan process. At a given wavelength  $\lambda$ , the image  $I$  is described over the field of view by

$$I = \text{PSF} \otimes O$$

where PSF denotes the instrument PSF,  $O$  the object angular intensity distribution, and  $\otimes$  the convolution operator. The corresponding image spatial spectrum  $\tilde{I}$  is equal to

$$\tilde{I} = \mathcal{F}(I) = \text{OTF} \cdot \tilde{O}$$

where OTF is the instrument optical transfer function,  $\tilde{O}$  the object spatial spectrum, and  $\mathcal{F}(I)$  the Fourier transform of the image  $I$ .

The PSF can be optimized for high-contrast imaging (see Fig. 1). This ability is characterized by the PSF dynamic range (DR), which is defined as the ratio between the PSF main peak intensity  $I_{\max}$  and the maximum intensity level  $I_{\text{DF}}$  over the PSF dark field (DF: the PSF area where residual side lobes are located):

$$\text{DR} = \frac{I_{\max}}{I_{\text{DF}}}$$

The object angular size must not exceed the array clean field of view (CLF) to avoid any aliasing effect. The clean field of view is defined as

$$\text{CLF} = \frac{\lambda}{B_{\min}},$$

where  $B_{\min}$  is the smallest array baseline. The dark field corresponds to the CLF area where a faint object could be detected.

Our main goal is to provide images with both high angular resolution and high contrast using a limited number of telescopes (fewer than ten). For this purpose, in a previous study (Armand et al. 2009), the telescope spatial distribution in the THT input pupil and the relative photon flux collected by each sub-aperture were optimized to maximize the dynamic range when imaging a high-contrast linear object, such as a star-planet system.

The THT test bench can be divided into four main parts (see Fig. 3).

- The binary-star simulator:  
The star simulator consists of two single-mode fibres fed by independent distributed-feedback (DFB) lasers at  $1.55 \mu\text{m}$  located in the focal plane of a lens. These sources are linearly polarized. The intensity ratio between the two point-like sources can be adjusted to set the intensity distribution of the object under test. Their angular separation is equal to  $25 \mu\text{rad}$ . In the framework of this experimental study, we only use quasi-monochromatic light.
- The telescope array:  
The telescope array consists of eight lenses acting as telescopes. The input pupil mapping is reported in Fig. 2. This configuration is equivalent to a redundant linear array when observing a binary star (i.e. 1D object along a vertical direction). By applying the apodization technique to maximize the dynamic range, the flux levels can be adjusted by an iris in front of each sub-aperture to fit the theoretical optimized configuration. The wavefront portions collected by each lens are then injected into single-mode polarization maintaining fibres. This leads to a spatial filtering (Lardière et al. 2007) and a control of the polarization of the optical fields along the beam propagation. The clean field of view is  $\text{CLF} = 62 \mu\text{rad}$ . The optimization was done for the following dark field area  $\text{DF} = [-31; -15.5] \cup [15.5; 31] \mu\text{rad}$ .
- The eight-arm interferometer:  
Each arm consists of a fibre delay line and a fibre optical path modulator. The first device enables the balancing of the optical path lengths between the interferometer arms. The second device enables the temporal modulation of optical path

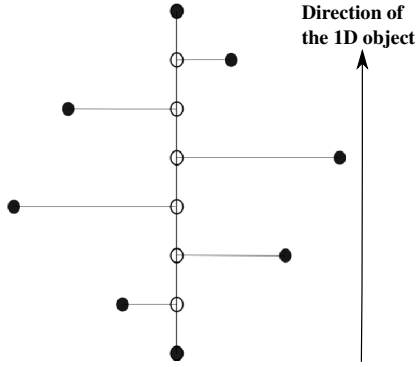


**Fig. 2.** Theoretical (white disks) and experimental (black disks) telescope array configuration. Owing to the experimental constraints, the configuration of the telescope array is not linear. However, the projection of the telescope baseline along the vertical axis (direction of the 1D object) is fully identical to the theoretical redundant configuration. These two configurations are equivalent to a 1D vertical array when observing a 1D vertical object.

required to achieve the image acquisition with the THT instrument. The optical path difference  $OPD_{kl}$ , generated between the arms  $k$  and  $l$ , is driven by the golden rule of imaging interferometry that requires a linear relationship between the telescope baseline and the related optical path difference:

$$OPD_{kl} = \lambda \frac{B_{kl}}{B_{\min}} \left( \frac{t}{t_0} - \frac{1}{2} \right),$$

where  $B_{kl} = (k - l)B_{\min}$  is the baseline between telescopes  $k$  and  $l$ , and  $t_0$  is the scan time of the entire clean field of view. The temporal modulation of optical paths allows acquisition of a single image (called the short-exposure image) every  $t_0 = 100$  ms. Finally, beams collected by each sub-aperture are mixed in an eight-to-one optical combiner.

- The signal acquisition and processing:

At the eight-to-one optical combiner output (see Fig. 4), the light is split into two channels by using a 90/10 Y optical junction creating high flux – low flux channels.

The first channel uses an InGaAs photodiode to directly detect the infrared high flux level. It is not used in the servo loop of the co-phasing system. In the second channel, the light passes through an adjustable fibre attenuator combined with a hybrid detector (Roussev et al. 2004), which reduces the  $1.55 \mu\text{m}$  light flux to the photon-counting regime and mimicks a real astronomical observation. The InGaAs detector at this infrared wavelength has a high dark-count level and a low detection efficiency. To overcome this problem, we used a hybrid detector developed in our laboratory (Ceus et al. 2012). This detector is based on a sum-frequency generation process used for its inherently noiseless properties (Louisell et al. 1961). In a non-linear optical waveguide (PPLN crystal) pumped by a  $1.064 \mu\text{m}$  YAG laser, the  $1.55 \mu\text{m}$  infrared light is converted into a  $633 \text{ nm}$  visible signal (see Fig. 5). This way, in the photon-counting channel, the signal can be acquired by a silicon photon-counting photodiode with a very low dark count (2.5 photons/frame).

Two channels are simultaneously recorded by the same data acquisition board. The first channel is a short-exposure high-flux image used as a reference measurement. The second channel records single-photon events captured by the photon-counting detector. Knowing the phase-modulation applied on the interferometer arms, the arrival time of each photon can be linked to an angular position in the image. Figure 4 illustrates such an acquisition.

### 3. Co-phasing in the photon-counting regime

#### 3.1. The principle of co-phasing process

The co-phasing system, previously implemented on the THT test bench, is based on a joint use of the sub-aperture piston phase diversity technique (SAPPD, Bolcar & Fienup 2005, 2009), and a genetic algorithm (GA, Brady 1985).

The phase diversity technique allows us to compute a phase criterion sensitive to the phase aberrations of the multi-aperture instrument, but independent of the unknown geometry of the astronomical target. This process involves acquiring two different images of the same object. The first one, called the standard image  $I_0$ , is the current image of the object for which the phase piston errors must be cancelled. The second one, called the diversity image  $I_d$ , is obtained by applying known aberration errors to the instrument.

On the THT test bench, the diversity function is generated using optical path modulators located on each interferometer arm. These variations between the optical paths are directly related to the piston phase. The piston diversity range (PDR) is the span over which the values of piston phase diversity are randomly chosen.

The two images are used to compute a phase criterion  $\chi^{\text{ref}}$  that does not depend on the target intensity distribution and that is a relevant signature of the actual piston errors. Kendrick et al. (1994) have proposed four different metrics to get the  $\chi^{\text{ref}}$  criterion

$$\begin{aligned} M_1(v_i) &= \frac{\tilde{I}_0(v_i)}{\tilde{I}_d(v_i)} \\ M_2(v_i) &= \frac{\tilde{I}_0(v_i) \cdot \tilde{I}_d^*(v_i) - \tilde{I}_d(v_i) \cdot \tilde{I}_0^*(v_i)}{\tilde{I}_0(v_i) \cdot \tilde{I}_0^*(v_i) + \tilde{I}_d(v_i) \cdot \tilde{I}_d^*(v_i)} \\ M_3(v_i) &= \frac{\tilde{I}_0(v_i) \cdot \tilde{I}_d^*(v_i) + \tilde{I}_d(v_i) \cdot \tilde{I}_0^*(v_i)}{\tilde{I}_0(v_i) \cdot \tilde{I}_0^*(v_i) + \tilde{I}_d(v_i) \cdot \tilde{I}_d^*(v_i)} \\ M_4(v_i) &= \frac{\tilde{I}_0(v_i) \cdot \tilde{I}_0^*(v_i) - \tilde{I}_d(v_i) \cdot \tilde{I}_d^*(v_i)}{\tilde{I}_0(v_i) \cdot \tilde{I}_0^*(v_i) + \tilde{I}_d(v_i) \cdot \tilde{I}_d^*(v_i)}, \end{aligned}$$

where  $\tilde{I}_0$  and  $\tilde{I}_d$  are the standard and diversity image Fourier spectra, respectively. Here,  $v_i = i \cdot B_{\min} / \lambda$  is one among the eight spatial frequencies sampled by the redundant telescope array,  $i$  varies from 0 to 7, and  $z^*$  denotes the complex conjugate of  $z$ . All these metrics are independent of the object because the object spectrum is simultaneously involved in the numerator and the denominator of each formula.

The whole phase criterion is computed with

$$\chi_j^{\text{ref}} = \sum_{v_i} M_j(v_i),$$

where  $j$  is the label of the metric. The value of the phase criterion  $\chi^{\text{ref}}$  has a non-linear relationship to piston errors in the instrument. The genetic algorithm is then used to solve this non-invertible problem.

This technique has been used to design and optimize a phased antenna array (Ares-Pena et al. 1999; Marcano & Durán 2000). The genetic algorithm principle stems from the Darwin evolution theory, where a population of individuals is confronted with its natural environment. The most-well adapted individuals with respect to their environment have greater chances of reproducing themselves and so transmitting their genotype. New individuals are obtained by crossing the genotype of two parents

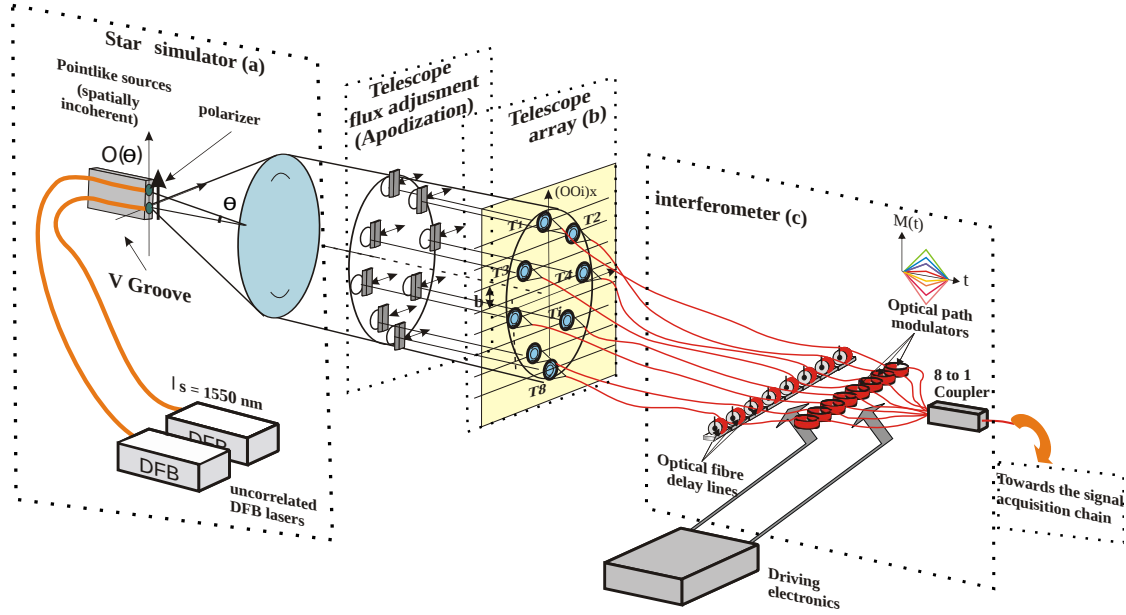


**Fig. 3.** Temporal hypertelecope test-bench scheme. This setup is divided into four main parts: (a) the unbalanced binary-star simulator, (b) the telescope array, (c) the eight-arm interferometer, and (d) the signal acquisition chain.

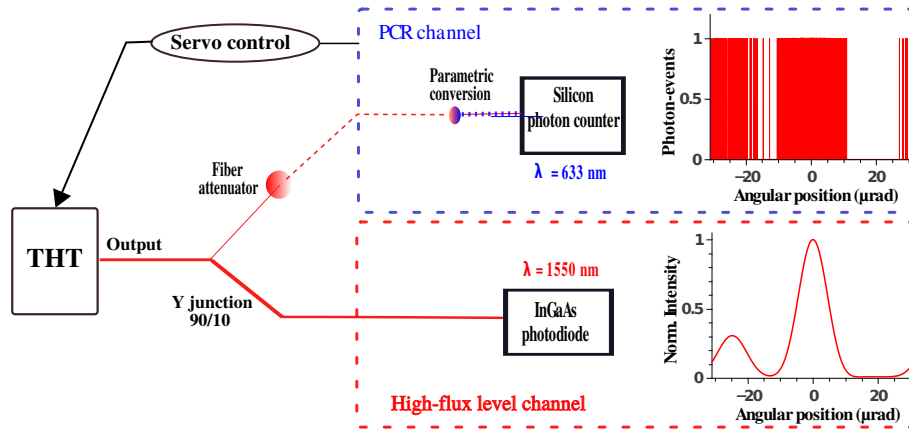


**Fig. 4.** Signal-acquisition chain. Two signals are simultaneously acquired. The first one (top curve) is a short-exposure image obtained in the photon-counting regime (PCR) by using a hybrid detector, the second one is the image simultaneously detected with a high flux level

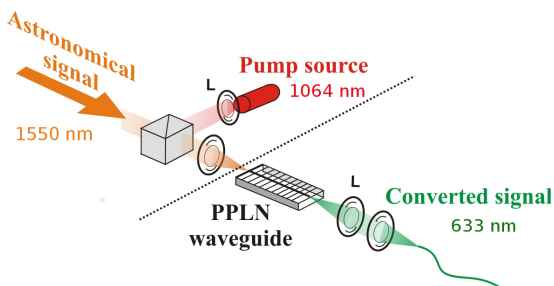


**Fig. 5.** Principle of the up-conversion by sum frequency generation. The beams coming from the pump source and the astronomical target are injected into a PPLN-waveguide. The infrared signal is converted into a visible signal that can be detected using a silicon photon-counting detector.

lengths linked to the interferometer arms are the only free parameters defining the genotype of an individual. In our instrument, a co-phasing cycle follows the sequence:

- image  $I_0^{\text{ref}}$  acquisition,
- random generation of piston phase diversity,
- acquisition of diversity image  $I_d^{\text{ref}}$ ,
- computation of the reference phase criterion  $\chi^{\text{ref}}$ ,
- sending  $\chi^{\text{ref}}$  and piston diversity values into the genetic algorithm,
- iterative evaluation of the piston errors with the genetic algorithm,
- adjustment of the optical path length in each interferometer arm.

Finally, a new cycle of co-phasing begins again.

(i.e. selected individuals of the previous generation). The genotype of this new individual can finally diverge from its parents by a mutation effect: each gene can acquire a modified value that is slightly different from its parents. In our case, the optical path

### 3.2. Selection of the most efficient metric

In a previous study using a high flux level (Bouyeron et al. 2012), we numerically tested the co-phasing efficiency of each

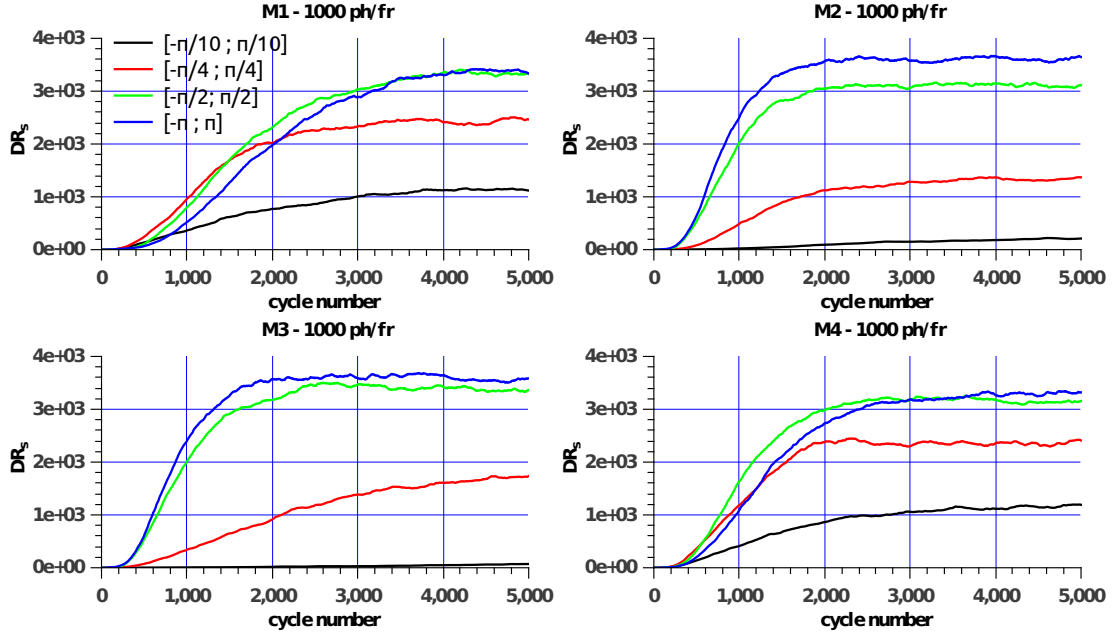


**Fig. 6.** Simulations of the dynamic range evolution  $DR_s$ , computed from the short-exposure images as a function of the number of cycles in the photon-counting regime for various pairs in the metric-phase diversity range. The number of photons per frame is close to 1000. The co-phasing algorithm works with the data from the channel operated in the photon-counting system.  $DR_s$  evolution is measured on high flux level data. In this framework, we assume that the THT is ideal (i.e. no more instrumental defects) and that only the photon noise corrupts the short-exposure image. The metrics  $M_2$  and  $M_3$  are more efficient than the  $M_1$  and  $M_4$  ones and require a large PDR  $[-\pi; \pi]$ .

metric for different phase diversity ranges  $([-\pi/10; +\pi/10], [-\pi/4; +\pi/4], [-\pi/2; +\pi/2], [-\pi; +\pi])$ . The metric's efficiency was evaluated through the dynamic range evolution ( $DR_s$ ) of the short-exposure image as a function of the number of co-phasing cycles. We observed that  $M_1$  and  $M_4$  were more efficient when applied with a narrow phase diversity range  $([-\pi/10; +\pi/10])$ , whereas  $M_2$  and  $M_3$  required a wide one  $([-\pi; +\pi])$ . Thus, to operate with high flux levels, each metric gives a similar performance when selecting their more suitable phase diversity range. Conversely, in the low flux regime, the photon noise affects the selection of the metric. This noise brings about additional random fluctuations of the intensity when short-exposure images are acquired. Figure 6 shows simulation results and illustrates the co-phasing behaviour for each metric at the low flux level. We demonstrate that when photon noise is significant, a wide phase diversity range gives the best results regardless of the metrics. Since  $M_2$  and  $M_3$  are intrinsically more efficient with wide phase diversity ranges, these two metrics lead to better performance in the photon-counting regime.

## 4. Data processing and experimental results

### 4.1. Experimental co-phasing tests of the temporal hypertelescope operating in the photon-counting regime

The purpose of this experimental study is to validate our co-phasing method dedicated to stabilize THT optical path lengths in the photon-counting regime. As a first step, the instrument target is a point-like source. According to the simulation results, we use the  $M_2[-\pi; \pi]$  metric for performing experimental tests. The co-phasing algorithm is fed by the data acquired on the photon-counting regime channel. To assess the efficiency of the co-phasing process, a short-exposure image is simultaneously acquired on the high flux level channel for each co-phasing cycle. The dynamic range evolution is extracted from these high

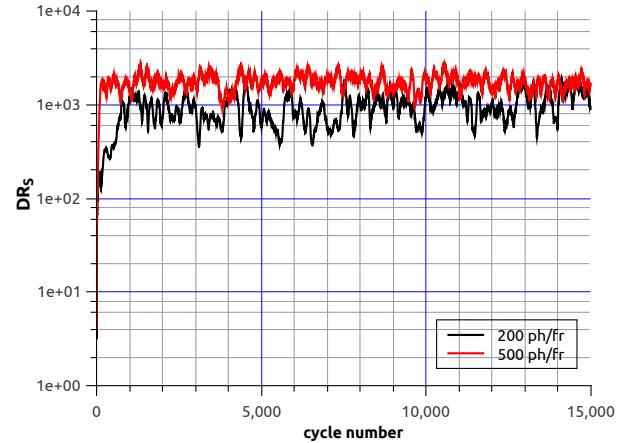


**Fig. 7.** Experimental dynamic range ( $DR_s$ ) evolution versus co-phasing cycle number obtained from the short-exposure images acquired with the THT test-bench operating in the photon-counting regime. The observed object is a point-like source. Two photon flux are investigated (200 and 500 photons/frame). The co-phasing algorithm works with the photon-counting regime data. The  $DR_s$  is measured with the high flux level data. The mean values of  $DR_s$  are equal to 1000 for 200 photons/frame and 1700 for 500.

flux data. Figure 7 shows the dynamic range evolution for two photon-flux levels (200 and 500 photons/frame). The averages of dynamic range obtained taking all short-exposure images into account are 1000 and 1700, respectively. Using the relationship between the dynamic range and the phasing error numerically computed through a Monte Carlo statistical approach (see Fig. 8), it is possible to plot the evolution of the residual error of the optical path difference (standard deviation of the OPD between the interferometric arms) in the instrument (see Fig. 9). The mean values of the OPD error are close to  $22.0 \pm 4.0$  nm

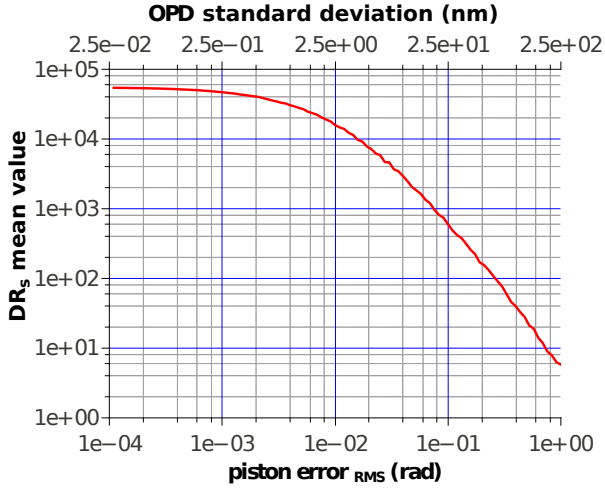


**Fig. 8.** Evolution of the average of the dynamic range value of short-exposure images as a function of the standard deviation of the phase piston (or OPD) between interferometer arms. This was numerically obtained through a Monte Carlo statistical approach. Each point is evaluated over 10 000 computed PSF. This curve is computed using the actual test-bench characteristics (apodization coefficients, array configuration, working wavelength, etc.). The only instrumental defect taken into account in this simulation is the piston phase error. For example, the  $DR_s$  mean value of 1000 corresponds to a 22 nm OPD standard deviation.

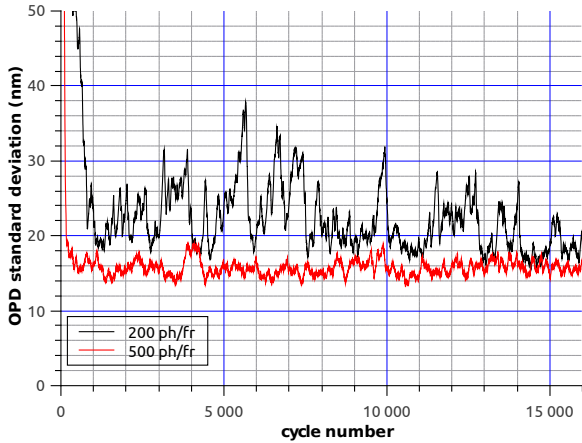


**Fig. 9.** Residual errors of the optical path difference experimentally observed during the acquisition of the THT point-spread function (here 25 min). These curves were obtained by using the relationship between the dynamic range and the RMS value of the OPD error (see Fig. 8). The mean values of the OPD standard deviation are close to 22 nm for 200 photons/frame and 15.7 nm for 500.

for 200 photons/frame and  $15.7 \pm 1.0$  nm for 500. These results demonstrate the feasibility of stabilizing the instrument's optical path lengths over a significant duration (here 25 min) with only a few hundred photons/frame detected at the output of the THT. Obviously, the co-phasing quality is lower than this one, which was previously obtained in high flux level (i.e. 4 nm, see Bouyeron et al. 2012), but as we see below, it is sufficient for acquiring high-contrast long-exposure images.

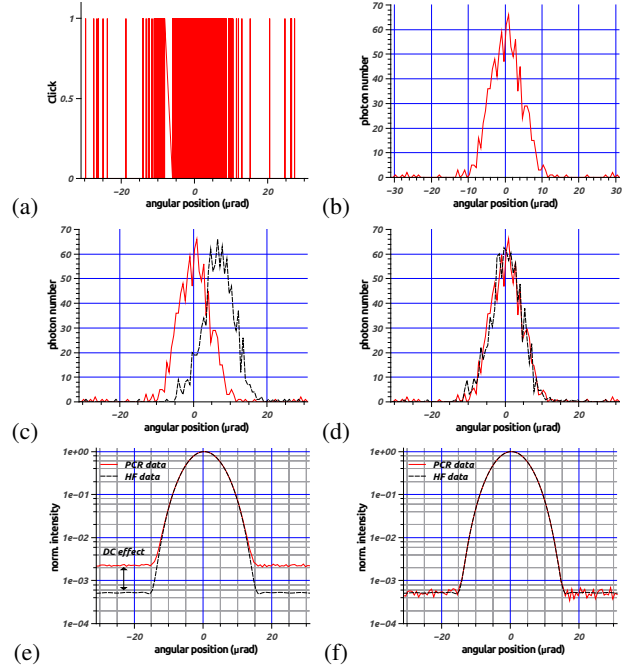


**Fig. 10.** Data reduction process: **a)** photon-counting regime frame; **b)** binned data; **c)** image before recentring and **d)** image after recentring; **e)** long-exposure images (photon-counting regime data and high-flux data) before dark count debiasing; **f)** long-exposure images after dark count debiasing.

## 4.2. Long-exposure image acquisition in the photon-counting regime

### 4.2.1. The different steps of the data reduction

The raw data acquired in the photon-counting regime cannot be used directly to get sharp images of the observed object. Data reduction is mandatory for obtaining high-contrast images. Figure 10 presents the different steps in this data processing. First, the photon frames (Fig. 10a) are converted from quantized data to analogue data by using a binning process. Each frame is converted in an  $N_p$  pixel image by adding together the photon-events detected over each sample (Fig. 10b). The object position in the image is a free parameter and can shift during the acquisition of successive frames. Therefore, in a second step, each image is recentred in the middle of the frame (Figs. 10c and 10d).

In a third step, the images are stacked to produce the long-exposure analogue image. Comparing the two long-exposure images simultaneously obtained with low and high flux levels, we observe a background shift between these two images (Fig. 10e). This gap is due to the photon-counting detector dark counts. This contribution is randomly superimposed on the photon frames and results in a homogeneous intensity background over long-exposure images. Finally, once we know the photon-counting detector's dark count rate, this bias can be removed and the two long-exposure images (resulting from the photon-counting regime and high flux level data) match perfectly (Fig. 10f).

One can observe a difference between the theoretical instrument PSF and experimental long-exposure image (see Fig. 11 left). This difference is due to the limited accuracy of the co-phasing process. Some photons are consequently incoherently superimposed on the coherent image (both on the photon-counting regime and high flux level channels). This phenomenon results in homogeneous noise on the whole image and can be removed by subtracting the mean value of this background (see

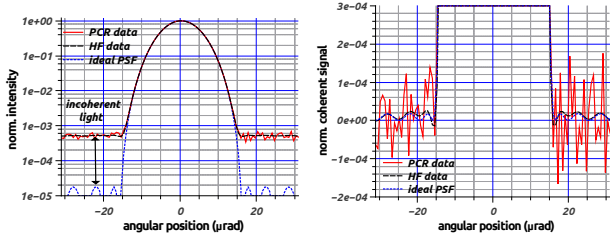


**Fig. 11.** Subtraction of the incoherent light. Due to the limited accuracy of the co-phasing process, a homogeneous background appears on the whole of the long-exposure image. The bias amplitude on a long-exposure image (left) is a function of photon-flux level and of number of short-exposure images. Its subtraction leads to an image close to the ideal PSF (right).

Fig. 11 right). The origin of this bias is mainly due to the photon noise limiting the co-phasing accuracy and to the limited resolution of the piezoelectric optical path modulator. The intensity bias to be subtracted is a function of the photon-flux level and is a reproducible process that can be evaluated by acquiring a calibration PSF.

Assuming that this background bias is mainly due to the photon count statistics, the noise behaviour on the dark field area can be analysed as follows. During a short-exposure image collecting  $N_{ph}$  photons per frame (see Fig. 12), the mean value of the background  $N_{sb}$  for each snapshot image can be approximately inferred from the snapshot dynamic range  $DR_s$ ,

$$N_{sb} \approx \frac{N_{ph}}{DR_s \cdot N_{pp}},$$

where  $N_{pp}$  corresponds to the number of pixels of the PSF peak. The full width at half maximum of this peak is about one-sixth of the clean field of view (CLF). Over an  $N_f$ -frame integration, we stack  $N_{ib} = N_f \cdot N_{sb}$  photon events on each pixel of the dark field. This number approximately corresponds to the background offset  $1/DR$  of the normalized long-exposure image and can be removed. Thus, the residual RMS fluctuation observed in each pixel of the dark field of the normalized long-exposure image is equal to

$$RMS = \frac{1}{DR \cdot \sqrt{N_{ib}}}.$$

#### 4.2.2. Image acquisition of an unbalanced binary star system

In this section, we report some experimental results obtained with the THT breadboard in the photon-counting regime. The co-phasing algorithm uses the  $M_2[-\pi; +\pi]$  metric. Two photon-flux levels have been investigated: 200 and 500 photons/frame. For each one, two long-exposure images have been acquired in the photon-counting regime: the instrument PSF, using a point-like source, and the image of an unbalanced binary system. In this second case, the companion was 1000 ( $\pm 10\%$ ) times weaker than the star. Figure 13 shows the comparison between a calibration PSF and the image of the binary star for the two photon-flux levels. These long-exposure images are obtained by stacking 30 000 short-exposure images for 200 ph/fr and 20 000 for 500 ph/fr. In both cases, the angular position and amplitude ratio between the main star and the companion are well measured (25  $\mu$ rad and factor 1000). The standard deviations of the intensity fluctuations measured on the PSF dark field are equal to  $1.1 \times 10^{-4}$  200 ph/fr and  $5.4 \times 10^{-5}$  for 500 ph/fr. If we only

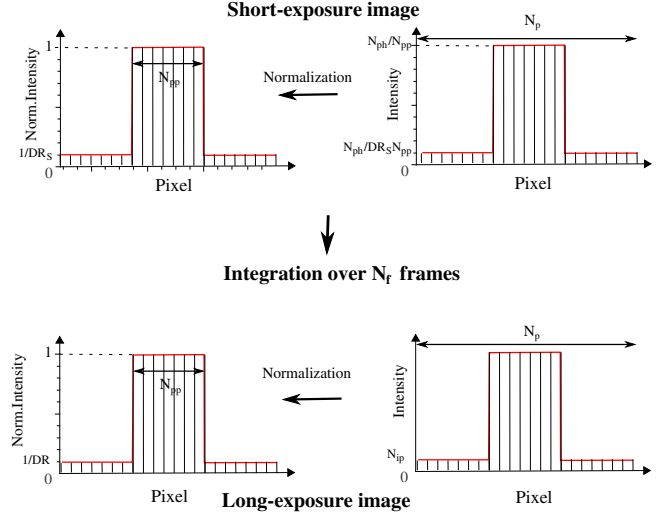


**Fig. 12.** Definition of the parameters required to estimate the intensity fluctuations in the dark field of the long-exposure image.

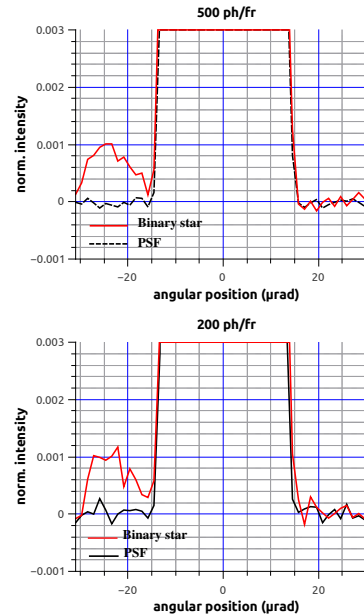


**Fig. 13.** Experimental images of a single star and a binary star obtained with the THT test bench in the photon-counting regime. Two photon flux are investigated (top: 500 and bottom: 200 photons/frame). The number of pixels is equal to 50 across the clean field of view. These images are obtained by stacking 30 000 and 20 000 short-exposure images for 200 and 500 ph/fr respectively. The intensity ratio between the two components of the unbalanced binary star is set to 1:1000 and their angular separation is 25  $\mu$ rad. The dynamic range (DR) of each long-exposure PSF measured before the background bias subtraction are close to 450 and 730 for 200 and 500 ph/fr, respectively.

consider the effect of the photon noise, the calculated RMS fluctuations are equal to  $8.3 \times 10^{-5}$  for 200 ph/fr and  $5.1 \times 10^{-5}$  for 500 ph/fr. These values are close to the measured intensity fluctuations and prove that the co-phasing process is mainly limited by the photon noise. The corresponding signal-to-noise ratio are 9000 and 18 000. The faint companion is at least ten times brighter than the noise observed experimentally. The signal-to-noise ratio value observed for 500 photons/frame reaches the limitation previously recorded with our co-phasing process using high flux data (Bouyeron et al. 2012). This limitation is

intrinsic to our test bench and is mainly due to the misalignment of the neutral axis of maintaining polarization fibre at each connection.

These experimental results demonstrate the imaging ability of the THT to properly operate in the photon-counting regime and, when using an appropriate data reduction process, the ability of this instrument to perform as well as in the high-flux regime.

## 5. Conclusion and discussion

Our previous study experimentally demonstrated the effectiveness of our system to co-phase an aperture synthesis instrument dedicated to direct imaging with a bright source. In this paper, we extend this performance even with the very weak photon-flux level in the range of the astrophysical sources. We optimized the algorithm parameters through numerical investigations (metric/PDR). By applying these parameters to our experimental setup, a stabilization of the OPDs in the range of 20 nm using only 200 photons per frame has been demonstrated experimentally. Using an averaging process over about 20 000 acquisitions and a data reduction method usable in the photon-counting regime, we produced high-contrast images of a (1:1000) unbalanced binary object. This measurement has been achieved with a signal-to-noise ratio equal to 10. This new experimental step demonstrates that the concept of hypertelescope is fully relevant for astrophysical applications.

For illustrative purposes, we extrapolated the results presented here to a large-scale and space-based instrument with the same architecture as our breadboard (linear array of eight telescopes in a redundant configuration). This case is close to our current setup with very low wavefront distortion before the telescope array and no variation in the baselines of the array as a function of time. A ground-based configuration would need to take the additional perturbations of the atmosphere and the geometric evolution of the baselines over the observation into account. We did not focus on the angular resolution specification that can be managed with the telescope-array configuration and the scale of the baselines. Therefore, the assumptions used in our extrapolation were as follows.

- The acquisition time of a single frame (short-exposure image) is set to 0.1 s.
- The operating wavelength is  $0.9 \mu\text{m}$  to directly benefit from both silicon photon-counting detectors and optical fibres. The reference spectral illuminance in *I* band is  $8.3 \times 10^{-13} \text{ W cm}^{-2} \mu\text{m}^{-1}$ . The mean energy per photon in this band is  $2.2 \times 10^{-19} \text{ J}$ .
- Global photometric losses are equal to 22 dB (coupling: 9 dB; polarization: 3 dB, apodization: 4 dB, insertion: 5 dB, detector quantum efficiency: 1 dB).
- With 200 photons per frame, the instrument is able to provide long-exposure images with a 1:10 000 contrast.
- The optical bandwidth is chosen equal to 100 nm. This assumption is made to allow the computation of the instrument

**Table 1.** Limiting magnitude for an unbalanced binary star observation.

$D$ (cm)	$M_s$	$M_c$
20	6.4	16.4
30	7.3	17.3
40	7.9	17.9
50	8.4	18.4

**Notes.**  $D$  is the diameter of the mirrors.  $M_s$  is the magnitude of the main star required to have 200 photons per frame.  $M_c$  is the limiting magnitude of the companion.

theoretical performance. However, it has not been tested yet on our test bench. This will be one of the next steps in our investigations.

This way, we can estimate the limiting magnitude of the instrument when observing an unbalanced binary star. This computation is done for various mirror diameters (20 to 50 cm) to be in agreement with reasonable trade-off for a space mission. Results are shown in Table 1. Here,  $M_s$  is the limiting magnitude of the main star, and  $M_c$  is the magnitude of its faint companion ( $\Delta m = 10$ ). These results show that, even for relatively small mirror diameters, such an instrument can obtain highly resolved and high-contrast images of stellar systems (Ollivier et al. 2009).

*Acknowledgements.* This work is supported by Thales Alenia Space and the Centre National d'Études Spatiales (CNES). We are grateful to A. Dexte for his suggestions regarding all the specific mechanical components.

## References

- Ares-Pena, F. J., Rodríguez-Gonzalez, J. A., Villanueva-Lopez, E., et al. 1999, IEEE Trans. on Antennas and Propagation, 47, 506
- Armand, P., Benoist, J., Bousquet, E., et al. 2009, Eur. J. Operational Research, 195, 519
- Brady, R. M. 1985, Nature, 317, 804
- Bolcar, M. R., & Fienup, J. R. 2005, Proc. SPIE, 5896, 1
- Bolcar, M. R., & Fienup, J. R. 2009, A. Opt., 48, A5
- Bouyeron, L., Olivier, S., Delage, L., et al. 2010, MNRAS, 408, 1886
- Bouyeron, L., Delage, L., Grossard, L., et al. 2012, A&A, 545, A18
- Ceus, D., Reynaud, F., Woillez, J., et al. 2012, MNRAS, 427, L95
- Lawson R. 1997, Selected Papers on Long Baseline Stellar Interferometry, SPIE Milestone Series (Washington)
- Kendrick, R. L., Acton, D. S., & Duncan, A. L. 1994, A. Opt., 33, 6533
- Labeyrie, A. 1996, A&ASS, 118, 517
- Lardièrre, O., Martinache, F., & Patru, F. 2007, MNRAS, 375, 977
- Louisell, O., Yariv, A., & Siegman, A. E. 1961, Phys. Rev., 124, 1646
- Marcano, D., & Durán, F. 2000, IEEE Antennas and Propag. Mag., 42, 12
- Ollivier, M., Absil, O., Allard, F., et al. 2009, Exp. Astron., 23, 403
- Patru, F., Tarmoul, N., Mourard, D., & Lardièrre, O. 2009, MNRAS, 395, 2363
- Petrov, R. G., Malbet, F., Weigelt, G., et al. 2007, A&A, 464, 1
- Reynaud, F., & Delage, L. 2007, A&A, 465, 1093
- Roussev, R. V., Langrock, C., Kurz, J. R., & Fejer, M. M. 2004, Opt. Lett., 29, 1449
- Ten Brummelaar, T. A., McAlister, H. A., Ridgway, S. T., et al. 2005, ApJ, 628, 453
- Traub, W. A. 1986, Appl. Opt., 25, 528